Journal of Environmental Chemical Engineering 14 (2026) 121922

Contents lists available at ScienceDirect

Journal of Environmental Chemical Engineering

journal homepage: www.elsevier.com/locate/jece

Phosphate recovery by struvite production from synthetic wastewater using a highly scalable 3D printed filter-press electrochemical flowcell

Benjamin Rommelhoff Høy [a], Soorena Gharibian [a,*], Massimiliano Errico [a,b], Knud Villy Christensen [a], Per Morgen [a]

[a] Chemical Engineering section, Department of Green Technology, Faculty of Engineering, University of Southern Denmark, Campusvej 55, Odense 5230, Denmark
[b] Department of Mechanical, Chemical and Materials Engineering, University of Cagliari, Via Marengo 2, Cagliari 09123, Italy

ARTICLE INFO

Keywords:
Wastewater treatment
Phosphate recovery
Struvite
Electrochemical process
Flowcell

ABSTRACT

This study demonstrates the continuous production of value-added struvite ($MgNH_4PO_4$) from synthetic wastewater at pre-pilot scale using a 3D printed filter-press electrochemical flowcell. The system was operated in full-recirculation mode for 3 hr at a flowrate of 0.62 L/min to create turbulent conditions in the reactor and across the electrode surfaces. Experiments were conducted at pH 8.5 at a current density of 1.7 mA/cm^2. An average PO_4^{3-} recovery of 85 % was achieved, with a struvite yield of 40 %. Precipitates formed on the anode (24 %), in the bulk solution (14 %), and on the cathode (2 %). Although struvite nucleates preferentially on the anode surface, results suggest that the turbulent flow induced partial detachment of struvite from the anode surface. The successful struvite formation was verified with attenuated reflectance-Fourier transform infrared (ATR-FTIR) spectroscopy, energy dispersive spectroscopy (EDS) in a scanning electron microscope (SEM), and X-ray diffraction (XRD). All these techniques showed good agreement with known pure struvite characteristics. The results suggest potential extension to industrial and municipal wastewater systems, with future studies addressing process optimization approaches aimed at mitigating anode passivation and enhancing struvite recovery. Overall, the results point to the flexibility and scalability of electrochemical filter-press flowcells for integration into continuous, green wastewater treatment and resource recovery systems.

1. Introduction

Phosphorus (P) is an indispensable nutrient for plant growth and food production, serving as a key component of fertilizers and is thus a cornerstone for global agriculture and food security. However, P is a finite Earth resource, with global mineable deposits unevenly distributed and limited. Estimates of when it will be "used up" vary widely, with analyses suggesting that, depending on consumption growth, deposit quality, and recycling rates, depletion could occur within decades or deposits will last for hundreds of years [1]. European dependence on imported P in rocks is already high, making the region particularly vulnerable to supply insecurity [2]. At the same time, municipal and agricultural wastewater streams contain high concentrations of organic matter, ammonium (NH_4^+), and P in the form of phosphate (PO_4^{3-}), which create environmental problems such as eutrophication [3]. Process wastewater generated during the thermal processing systems, like hydrothermal liquefaction (HTL) of various biomass feedstocks, including algae and sewage sludge, contains high concentrations of NH_4^+ and PO_4^{3-} [4,5]. Instead of being viewed solely as pollutants, these streams can be looked at to represent promising secondary P sources. Appropriate recovery and management can help reduce eutrophication of surface waters while simultaneously contributing to circular P use and resource security [6]. It is estimated that approximately 20–22 % of the world's P consumption could potentially be recovered through the right wastewater treatment [7–9]. Common recovery methods from wastewater include adsorption, membrane processes, precipitation, biological treatment (followed by thermochemical sludge treatment), and crystallization [10,11].

Among the different recovery strategies, struvite ($MgNH_4PO_4{\cdot}6\,H_2O$) crystallization has gained attention over the past decade as a viable method for PO_4^{3-} recovery from wastewater, sludge liquors, and manure [7,12–17]. Struvite is a poorly soluble mineral that forms stable, white orthorhombic crystals, which often precipitate spontaneously in pipelines and sludge treatment equipment, causing operational problems

* Corresponding author.
E-mail address: sog@igt.sdu.dk (S. Gharibian).

https://doi.org/10.1016/j.jece.2026.121922
Received 9 January 2026; Received in revised form 20 February 2026; Accepted 21 February 2026
Available online 23 February 2026

and increasing maintenance costs [7,9,18]. However, this deposit can be turned from a problem into an opportunity, if recovered, since struvite is a slow-release, premium-grade fertilizer with recognized agronomic value and economic potential [19,20].

Struvite precipitation occurs optimally when magnesium (Mg^{2+}), NH_4^+, and PO_4^{3-} are present in equimolar, fully mineralized concentrations under supersaturated conditions [7,18,21]. The overall reaction is given in Eq. 1:

$$Mg^{2+} + NH_4^+ + H_nPO_4^{n-3} + 6H_2O \rightarrow MgNH_4PO_4 \cdot 6H_2O \downarrow + nH^+ \quad (1)$$

where n = 0, 1, 2, depending on solution pH.

Conventional chemical precipitation relies on the continuous supply and storage of external chemicals (e.g., Mg salts), which increase operational costs and the environmental footprint associated with chemical production and transport. This is not considered a sustainable approach [7,13,22]. In contrast, electrochemical struvite precipitation employs a sacrificial Mg anode to supply Mg^{2+} *in-situ* via anodic dissolution, eliminating the need for external Mg dosing and reducing chemical sludge generation. Moreover, unlike conventional chemical precipitation, electrochemical systems can operate without external pH adjustment, as the required pH increase is achieved *in-situ* through water reduction at the cathode. This simultaneous *in-situ* control of Mg^{2+} availability and pH enhance process efficiency, lowers chemical consumption, and operational costs. While chemical precipitation is well established, it is often associated with high reagent demand and potential secondary pollution from residual chemicals. Electrochemical precipitation primarily relies on electrical energy input, offering improved sustainability potential, particularly when coupled with renewable energy sources [9,23,24]. Mg–air cells offer the advantage of enabling nutrient recovery without external Mg salt addition while providing concurrent electricity generation. These cells however rely on corrosion-driven Mg dissolution coupled with oxygen reduction, where Mg^{2+} release, local pH evolution, and supersaturation are uncontrolled and governed by corrosion chemistry and oxygen mass transfer rather than externally controllable process variables [13,25]. The main reactions governing Mg^{2+} dissolution, hydroxide generation, and struvite precipitation in a system derived by electrical energy consumption for struvite production are listed in Eq. 2–4:

$$\text{Anode}: Mg(s) \rightarrow Mg^{2+}(aq) + 2e^- \quad (2)$$

$$\text{Cathode}: 2H_2O\ (l) + 2e^- \rightarrow 2OH^-(aq) + H_2(g) \quad (3)$$

$$\text{Struvite formation}: Mg^{2+}(aq) + NH_4^+(aq) + PO_4^{3-}(aq) + 6H_2O(l) \rightarrow MgNH_4PO_4 \cdot 6H_2O\ (s) \quad (4)$$

Sultana et al. [14] showed that with synthetic wastewater ($NH_4H_2PO_4$ precursor) and using a batch/beaker scale reactor, after 6 hr, the electrochemical struvite precipitation results in more than 90 % PO_4^{3-} removal, particularly at pH 8–10 under enhanced salinity (NaCl), which leads to higher sacrificial Mg anode dissolution. In another approach, Zhou et al. [16] integrated a two-phase electrochemical system using batch/beaker scale reactors for simultaneous PO_4^{3-} and NH_4^+ removal from the supernatant of the hydrolysis sludge. Their results indicated that during Phase I, electrochemical precipitation using a magnesium sacrificial anode achieved removal efficiencies of 92.3 % for PO_4^{3-}-P and 50.1 % for NH_4^+-N at pH 9.0 and a current of 40 mA after 120 min of electrolysis. In Phase II, the remaining NH_4^+-N was further indirectly electro-oxidized to N_2 using a modified Ti anode (Ti/SnO_2–Sb–Pd). With the generation of active chlorine, approximately 83.2 % of NH_4^+-N was removed at a Cl/N molar ratio of 5:1 and a current of 50 mA after 120 min of treatment. Finally, the integrated process was operated under the optimal conditions (pH 9.0, I = 40 mA in Phase I; Cl/N = 5, I = 50 mA in Phase II), achieving NH_4^+-N and PO_4^{3-}-P removals of 79.3 % and 94.3 %, respectively. In a study by Nagy et al. [26], a scaled-up single-cell electrochemical batch reactor with a working volume of 16 L was developed to investigate how progressive Mg anode deterioration affects struvite formation and energy consumption over extended operation. A synthetic wastewater ($NH_4H_2PO_4$ precursor) was treated, and struvite precipitation was evaluated over six consecutive batch runs (6 hr per batch run). Overall, the scaled-up reactor achieved higher P recovery efficiencies (40–54 %) compared to their previously reported laboratory-scale setup (38 %). However, as the number of batches increased, struvite output declined markedly from approximately 320–210 g/batch, while electrical energy demand rose from 0.9 to 1.6 kWh/batch, primarily due to extensive Mg anode degradation. In total, approximately 1.6 kg of high-purity struvite was generated over six successive batch runs, with a specific energy consumption of 4.6 kWh/kg. In a recent study, Nagy et al. [13] have used an "open" flow reactor as an electroless Mg-air cell (0.75 L working volume) with inflow and outflow nozzles for struvite production from farm wastewater. The wastewater flowrate was 176 mL/min. Over a 3 hr experiment, the flow reactor achieved up to 87 % PO_4^{3-} and 77 % NH_4^+ removal, resulting in improved effluent quality. The produced electricity (maximum open-circuit voltage, ca. −1.8 V, and maximum current, ca. −80 mA) decreased over time due to the formation of a passivation layer and H_2 bubbles on the Mg anode. While flow reactor designs [13,27] demonstrate feasibility, they are not hydraulically optimal due to stagnant zones and large residence time, a large footprint, and a lack of scalability.

Together, batch/beaker scale studies provide strong evidence that electrochemical struvite recovery is feasible, but they also reveal challenges associated with batch/beaker-type reactors, including reactor optimization, continuous operation, formation of a struvite passivation layer on the anode, electrode cleaning/maintenance, and scalability. The filter press flowcell design widely used in literature for various other types of electrochemical processes [28–32] reflects the stack configurations widely applied in industrial electrolysis, including chlor-alkali processes [33] and water electrolysis for hydrogen production [34]. It offers proven scalability (i.e., multi-stack systems and reactors-in-series concept), efficient mass transfer, and compact design. Electrochemical flowcell reactors enable precise control of hydrodynamics and residence time distribution, and improve mass transfer. Flowcells can supply Mg^{2+} more uniformly, reduce passivation through controlled turbulence, and enable continuous treatment at variable scales based on the influent flowrate. Importantly, renewable electricity can power such electrochemical flowcells [13,15], enabling green/sustainable nutrient recovery in the form of valuable products, even from scrap Mg metals acting as sacrificial anode [7,16]. This integration links P recovery directly to Power-to-X and circular-economy energy platforms. Despite extensive research on electrochemical struvite precipitation, most existing studies are limited to batch or beaker-type reactors, which do not adequately represent the hydrodynamic, operational, and scalability challenges of continuous wastewater treatment systems. In particular, the practical application of an economical filter-press electrochemical flowcell operated in continuous mode for simultaneous PO_4^{3-} recovery and wastewater treatment has not yet been investigated. This gap limits the scale-up potential of the electrochemical struvite recovery process. The objective of the present study is, therefore, from a process engineering perspective, to evaluate the feasibility of continuous electrochemical struvite production using a cost-effective filter-press flowcell configuration. The underlying hypothesis is that a flowcell reactor offers improved hydraulic efficiency with minimal pressure drop, and enables a controlled, continuous electrochemical dissolution of a sacrificial Mg anode in a cost-effective and environmentally friendly manner. The enhanced hydrodynamics within the flowcell are expected to promote the detachment of struvite precipitates from electrode surfaces, thereby limiting passivation and reducing the need for frequent anode maintenance. To address these objectives, synthetic wastewater was treated in a 3D-printed, low-cost filter-press electrochemical flowcell equipped with a magnesium alloy (AZ31B) anode and a steel cathode, which was operated at the pre-pilot scale in full recirculation mode. Despite the

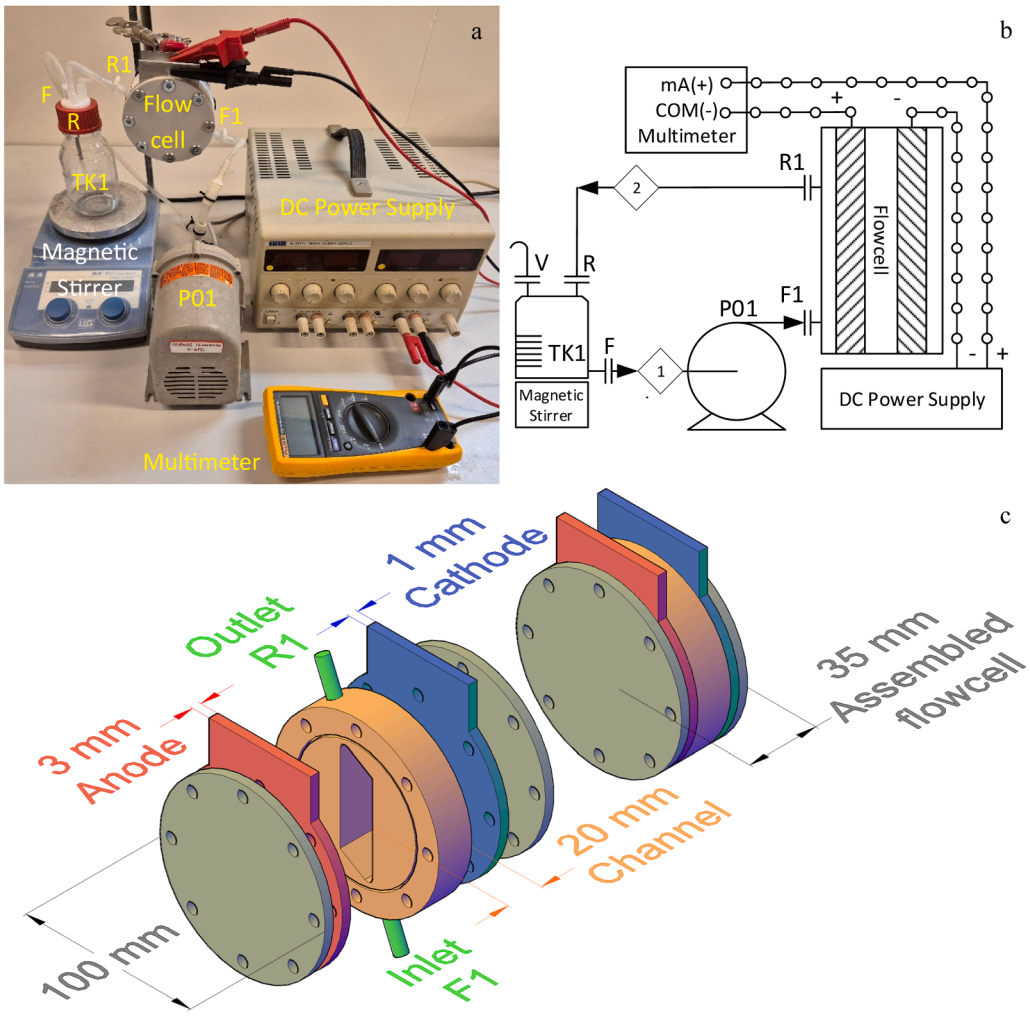

Fig. 1. a) Pre-pilot setup, b) PID, and c) Exploded and assembled view of the flowcell with dimensions. Abbreviations: TK1: feed reservoir, V: vent, F: feed nozzle, R: recirculation nozzle, PO1: recirculation pump, F1: flowcell inlet nozzle, R1: flowcell outlet nozzle. Streams: 1: feed from TK1 to flowcell, 2: flowcell outlet to TK1 in total recirculation mode.

complexity of electrochemical struvite production and PO_4^{3-} recovery, this study's findings indicate that continuous flowcells could effectively be incorporated into sophisticated wastewater treatment facilities. Given the modular nature of electrochemical flowcells, a scale-up of the proposed system to evaluate the treatment of real wastewater could be an interesting future research agenda.

2. Materials and methods

Deionized (DI) water (conductivity: < 1 μS/cm) from a PURELAB Chorus 1 system (ELGA LabWater, Veolia Water Technologies, France) was used in all experiments. NaOH, $(NH_4)_2HPO_4$ (≥98 %), Na_2SO_4 (≥99 %), Citric acid (98 %), and H_2SO_4 (98 %) were bought from Sigma-Aldrich (Germany). Pure struvite ($MgNH_4PO_4.6H_2O$, 98 %) was purchased from Alfa Aesar (USA).

Table 1
Flowcell dimensions and process general information.

Parameter (unit)	Value
Channel width (cm)	2
Channel diameter (cm)	10
Effective electrode area (cm^2)	11.6
Flowcell channel volume (mL)	23.2
Influent volume (mL)	200
Influent PO_4^{3-} concentration (mg/L)	1100
Initial influent pH	8.5
Initial influent conductivity (mS/cm)	3
Recirculation flowrate (L/min)	0.62
Operating temperature (°C)	25
Current density (mA/cm^2)	1.7

2.1. Experimental setup

Electrochemical struvite production tests were conducted using a 3D printed filter-press flowcell. The schematics of the setup are provided in Fig. 1a-c. An anode of 3 mm thickness made of AZ31B-Mg alloy (Evek GmbH, Denmark branch) and a cathode of 1 mm thickness made from steel. Before each test, electrodes were rinsed with DI water and gently abraded with an abrasive sponge to minimize surface oxides and contaminants. They were subsequently rinsed with ethanol to remove grease and dried with tissue paper. A DC power supply (EL302Tv, Aim-TTi, England) was connected to the electrodes, and the precise current was measured with a multimeter (179 True RMS, Fluke, USA). The 2 cm thick flow channel, without an inlet flow distributor and an outlet manifold to affect the flow distribution pattern, provided an effective electrode area of 11.6 cm^2. For the full recirculation mode tests, synthetic wastewater was fed to the system using a GL-45 250 mL bottle (TK1), which served as a reservoir, and a centrifugal pump (P01, Type 1031, Eheim, Germany) recirculated the wastewater at a rate of 0.62 L/min (Reynolds number of ca. 500 [29]). It is worth mentioning that

according to available literature [35,36], a large flowrate promotes turbulence/mass transfer inside flowcells, which in turn leads to a higher reaction rate. However, the effect of flowrate as an operational parameter was not further investigated. The wastewater flowed upward over the electrodes. Leak-tight operation was ensured by installing silicone rubber gaskets between the flow channel and electrodes and assembling the flowcell using bolts and nuts. The 3D printed flowcell body parts and channel were made of 2.85 mm PLA commercial 3D printing filaments (3deksperten, Denmark) using a commercial 3D printing device (S5, Ultimaker, Netherlands). 3D Printer settings were as follows: infill: 100 % with ZigZag pattern, supported printing, raft type build plate adhesion, speed: 100 mm/s, cooling fan speed: 100 %, layer height: 0.06 mm, number of top/bottom layers: 17, printing temperature: 200 °C, heated bed temperature: 60 °C. Table 1 presents a summary of flowcell dimensions and system parameters.

2.2. Process description

A 200 mL batch of synthetic wastewater, containing 1100 mg/L of $(NH_4)_2HPO_4$ and Na_2SO_4 as the supporting electrolyte (final conductivity of 3 mS/cm), was placed in the circulation reservoir. The pH was adjusted to 8.5 using diluted aqueous solutions of H_2SO_4 and NaOH. pH= 8.5 was selected based on literature [13,17] and the optimal range for struvite precipitation (pH=7–9). This minimize formation of impurities. In addition, considering $NH_4^+ \Leftrightarrow NH_3$ equilibrium (pK_a=9.25), operation at pH= 8.5 limits the conversion of NH_4^+ to volatile NH_3, which does not contribute to the struvite formation reaction [37,38]. To ensure uniformity, the wastewater in TK1 was continuously stirred using a magnetic stirrer. Once a steady flowrate was reached, the DC power supply was turned on. The flowcell was operated galvanostatically at 1.7 mA/cm, corresponding to 20 mA, with the applied voltage adjusted as needed to maintain the target current density throughout operation. This current density was selected based on values reported in the literature [7,14] and further supported by a series of preliminary batch experiments to minimize impurity formation (*vide infra*). At 20 min intervals, the power supply was switched off, followed by the pump (P01). The liquid retained in the pump head and reactor was drained back into the TK1. Voltage, current, pH, and conductivity were recorded simultaneously at every interval. After pH readjustment, P01 was restarted to reestablish flow, and the power supply was switched on to resume galvanostatic operation. This procedure was repeated throughout the 180 min experimental period. After 180 min, the power supply was switched off while P01 continued operating for an additional 10 min to flush the reactor. At the end of the operation, a 5 mL aliquot was withdrawn from the reservoir to determine the residual PO_4^{3-} concentration. The flowcell was then disassembled, and the electrodes allowed to dry in a desiccator for 24 hr before the precipitated solids were collected by gentle scratching using a stainless-steel spatula. The remaining reservoir solution was vacuum filtered through a 1.2 μm cellulose nitrate membrane (Sartorius, Germany), and the recovered solids were dried in a desiccator for 24 hr. The test was performed in triplicate, and the average value, along with standard error (SE), is reported for the yield and recovery according to Eqs. 5 and 6:

$$yield, \% = \frac{m_{experimental}}{m_{theoretical}} \times 100 \quad (5)$$

$$PO_4^{3-} recovery, \% = \frac{C_{influent} - C_{effluent}}{C_{influent}} \times 100 \quad (6)$$

Where $m_{theoretical}$ is the PO_4^{3-}-limited stoichiometric maximum struvite yield (Eq. S1 in the supplementary information) [g], $m_{experimental}$ is the mass of recovered solid precipitates [g], and $C_{influent}$ and $C_{effluent}$ are the concentration of PO_4^{3-} [mg/L] in the synthetic wastewater feed and in the solution of TK1 after 3 hr of continuous flowcell operation, respectively. Between triplicate tests, the reactor was cleaned by circulating 200 mL of a 5 wt% citric acid solution for 30 min, followed by rinsing with dilute NaOH in deionized water until a neutral pH was reached. For each test, a new set of electrodes was used to avoid biased performance comparison due to contamination and pitting corrosion of the Mg anodes.

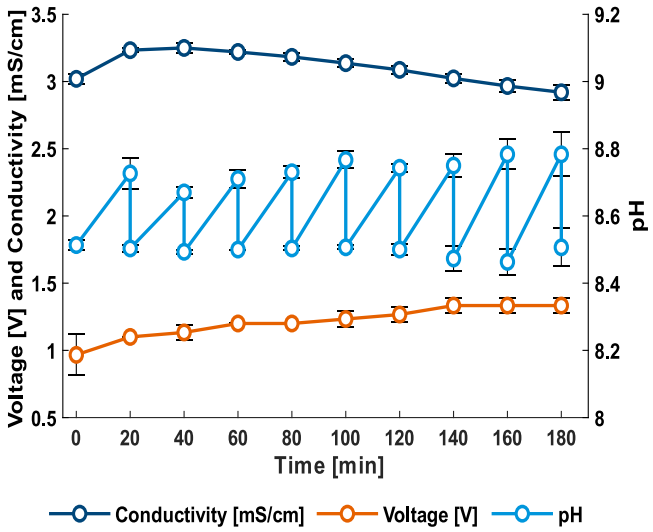

Fig. 2. Change in conductivity, voltage, and pH during 3 hr of continuous flowcell operation. Error bars represent SE (n = 3). Experimental conditions: Current density= 1.7 mA/cm^2 (20 mA), Initial pH= 8.5, Recirculation flowrate: 0.62 L/min.

2.3. Analytical methods

DR3900 spectrophotometer (HACH, USA) and LCK049 kits (HACH-Lange, Germany) were used for PO_4^{3-} concentration measurement without further sample dilution. A portable multimeter (HQ40d, HACH, USA) was used for measurement of pH (using PHC101 electrode), and conductivity (using CDC401 electrode). An attenuated total reflectance-Fourier transform infrared spectroscopy (ATR-FTIR) instrument (Cary 630, Agilent, USA) was used to obtain FTIR spectra of precipitates. The spectrum was recorded in the range 650–4000 1/cm at one 1/cm scan resolution (8 sample scans) in absorbance mode. A scanning electron microscope coupled with energy-dispersive spectroscopy (EDAX Elements in a SEM, Quanta200, FEI) was used for the crystal morphology evaluations and for obtaining EDS spectra/dot mapping at 5 kV (SEM) and 20 kV (EDS) without metal coating. Normal SEM images were recorded with an Everhard-Thornly secondary electron detector with a bias of + 300 V. To prevent damage to the SEM equipment from the evolution of gases during insertion in the vacuum, samples were first dried in a desiccator overnight. X-ray diffraction (XRD) analysis was performed with a MiniFlex 600 instrument (Rigaku, Japan). Diffraction patterns were collected over a 5–90° 2θ range with a step size of 0.02° and a scan speed of 10°/min, under Cu Kα radiation at 15 mA/40 kV operating current/voltage. XRD patterns of reference materials were calculated using VESTA v.3.5.8 [39] based on CIF files obtained from the Crystallography Open Database [40]. Rietveld refinement and relative phase purity were assessed using Profex v5.6.1 [41–43].

3. Results and discussion

3.1. Wastewater treatment performance

Overall, the replicate experiments exhibited low variation (Fig. 2), which was expected given the controlled/constant process parameters. This low variation was observed with the synthetic solution used, whereas higher variability is to be expected for complex wastewater effluents [13]. The conductivity of the solution inside TK1 increased

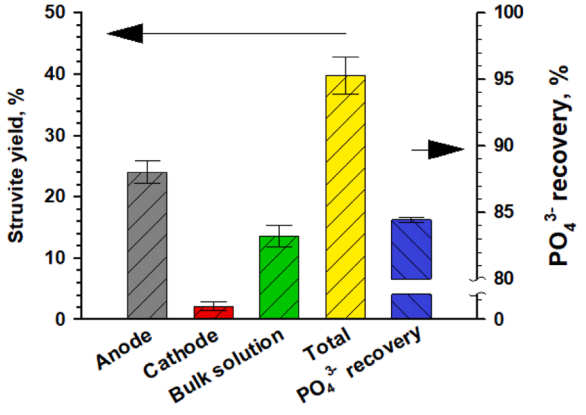

Fig. 3. Electrochemical struvite production yield and PO_4^{3-} recovery after 3 hr continuous flowcell operation. Error bars represent SE (n = 3).

during the first 20 min due to low reaction extent and the addition of acid for pH adjustment. After this point, the conductivity gradually decreased. The decline was stronger than the temporary increases caused by subsequent acid additions. This trend is consistent with the progressive precipitation of solids, which removes ionic species from the solution and therefore reduces conductivity. The corresponding rise in cell voltage correlates with the decrease in conductivity. Under galvanostatic operation, a gradually declining conductivity increased the cell resistance, and a higher voltage was therefore gradually required to maintain the set current. A secondary contribution to the increased voltage was attributed to the gradual thickening of the passivation layer on the electrodes (Fig. S1), which further increased resistance over time. The pH profile showed that the system naturally drifted toward alkaline conditions, driven by cathodic OH^- generation similar to what is reported in the literature [7,12]. Despite this tendency, pH was maintained close to 8.5 and never exceeded 9.0. Maintaining the pH within this narrow window limited the risk of forming competing co-precipitates and maintains conditions favorable for selective struvite precipitation [12,16]. A key competing phase is brucite ($Mg(OH)_2$), which forms readily at higher pH [11,14]. The likelihood of forming co-precipitates increases when the pH deviates from the optimal range of approximately 7–9 [44]. The risk of co-precipitate formation further increases when complex wastewater matrices are used, as the presence of competing ions such as Ca^{2+} has been shown in previous studies to promote the formation of secondary precipitates, thereby reducing the struvite yield [13,44]. Since the pH in this study never exceeded 9, there was sufficient operational margin to allow pH adjustments every 20 min without risking uncontrollable formation of undesirable precipitates in the synthetic solution. Based on the observed pH stability, less frequent pH adjustments would likely have been sufficient. However, in full scale electrochemical struvite production, automated pH adjustment in a buffer/conditioning feed tank, using a pH controller and a dosing pump, would be the standard solution to minimize competing co-precipitation and ensure favorable conditions for selective struvite formation.

Continuous operation of the flowcell resulted in 84.4 ± 0.2 % PO_4^{3-} recovery. The yield of struvite precipitates formed on the anode, cathode, and in the bulk solution was 24 ± 2 %, 2.1 ± 0.7 %, and 14 ± 2 %, respectively (Fig. 3, for weight distribution refer to Fig. S2). Summation of these contributions resulted in a total average recovered yield of 40 ± 3 %. This low yield is likely attributed to low extent of reaction, losses of precipitated struvite within the system, including retention in the hydraulic parts (Fig. S3), deposition on internal surfaces, and incomplete recovery from scratching the electrodes (Fig. S1). Such losses are consistent with previous literature, which reports that struvite readily precipitates on reactor surfaces and internal components [12]. Additionally, visual inspection revealed that struvite residues remained attached to the electrodes after operation but adhered too strongly to be

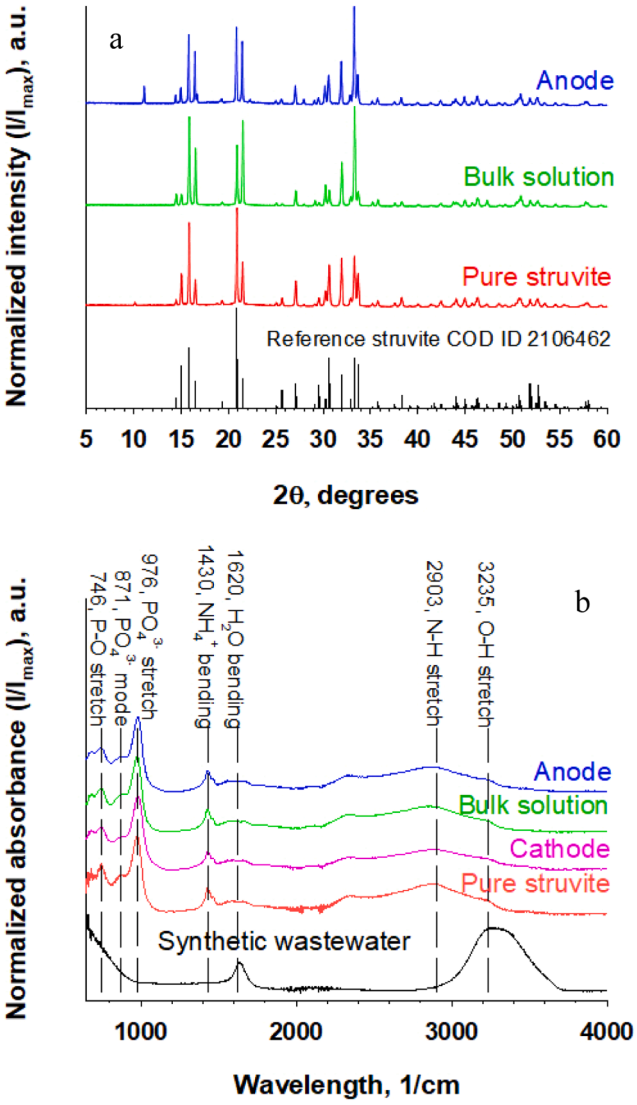

Fig. 4. a) XRD patterns of pure struvite, obtained precipitates, and reference struvite (COD ID 2106462). b) ATR-FTIR spectra of pure struvite, synthetic wastewater, and the obtained precipitates after 3 hr continuous flowcell operation.

removed by mechanical scratching (Fig. S1). This further supports the claim that incomplete physical recovery, rather than incomplete precipitation, accounts for the lower mass-based yield. It should be noted that complete conversion of PO_4^{3-} to struvite was not expected under the applied operating conditions and 3 hr of continuous flowcell operation. Calculations based on Faraday's law (Eqs. S1 and S2) and assuming 100 % current efficiency and ideal electrode behaviour indicated that a maximum of ca. 68 % struvite formation could be achieved due to the rate of Mg^{2+} release via electrochemical dissolution. In addition, preliminary batch/beaker scale experiments demonstrated that PO_4^{3-} recovery becomes increasingly kinetically limited at lower concentrations and requires longer process time (results not shown here). Together, these factors indicate that operation time and kinetics play a critical role in process optimization, as they directly influence both Mg^{2+} availability and struvite formation. However, prolonged operation must be carefully optimized to avoid excessive Mg^{2+} release, which could introduce secondary challenges/impurities when treating real wastewater streams.

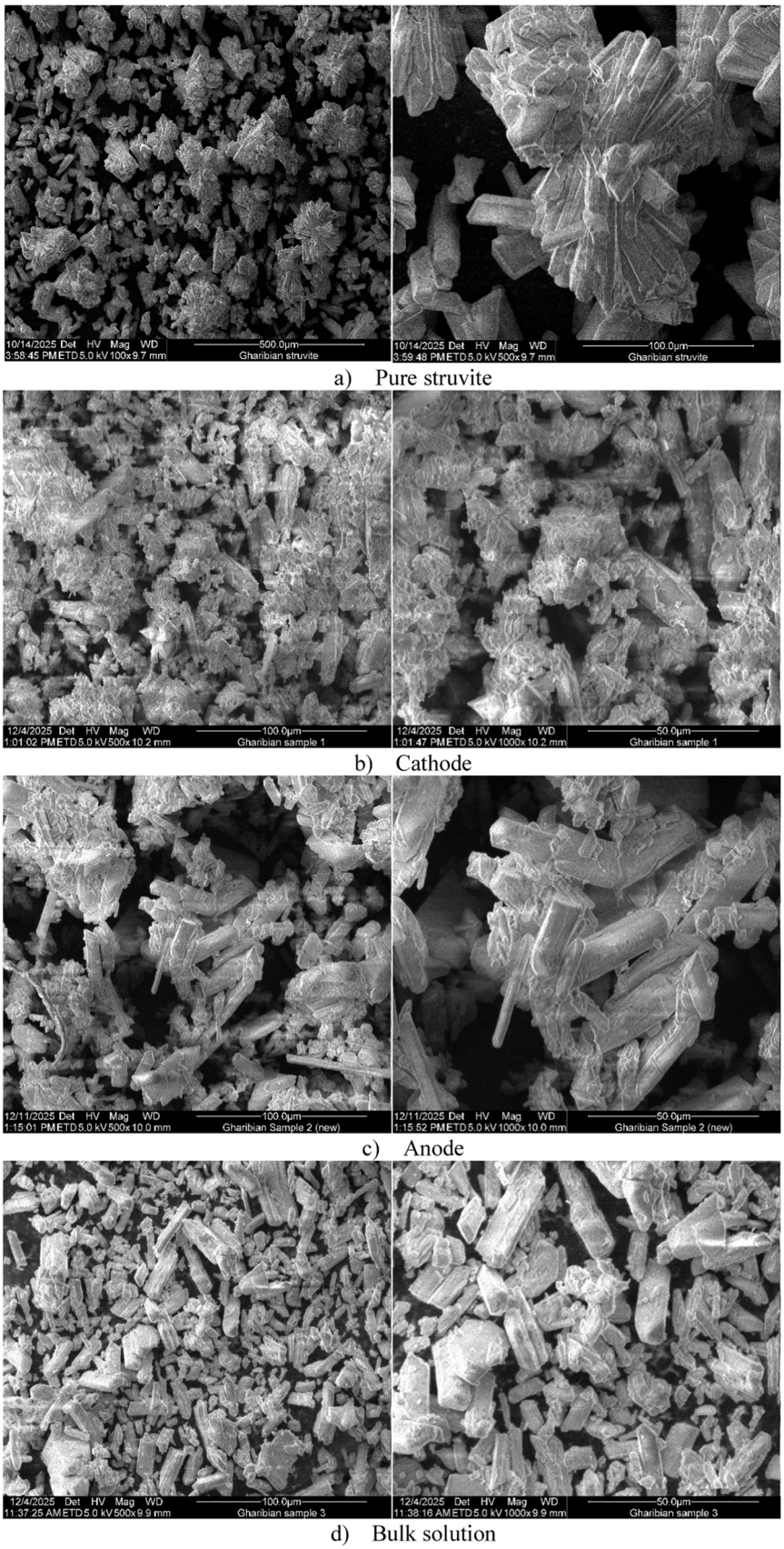

Fig. 5. SEM of pure struvite and obtained precipitates after 3 hr continuous flowcell operation.

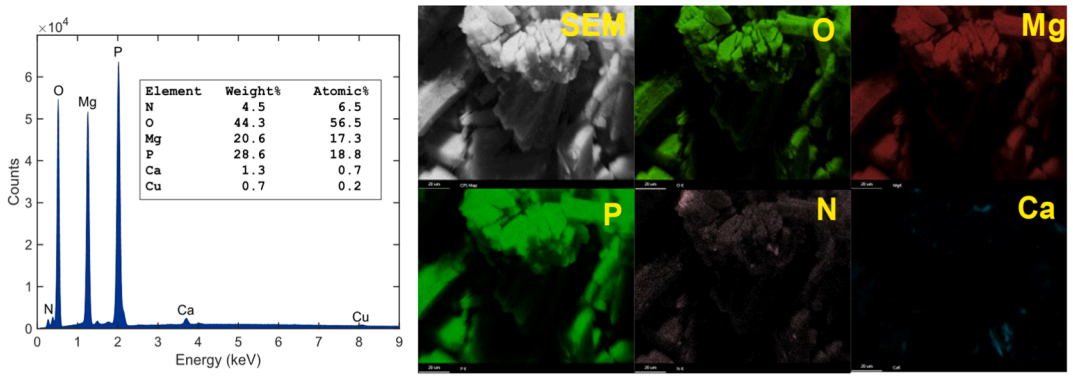

a) Pure struvite

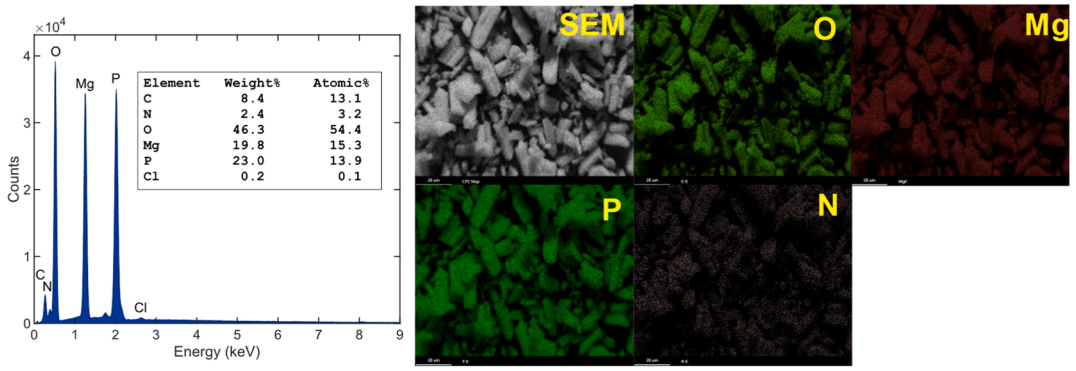

b) Bulk solution

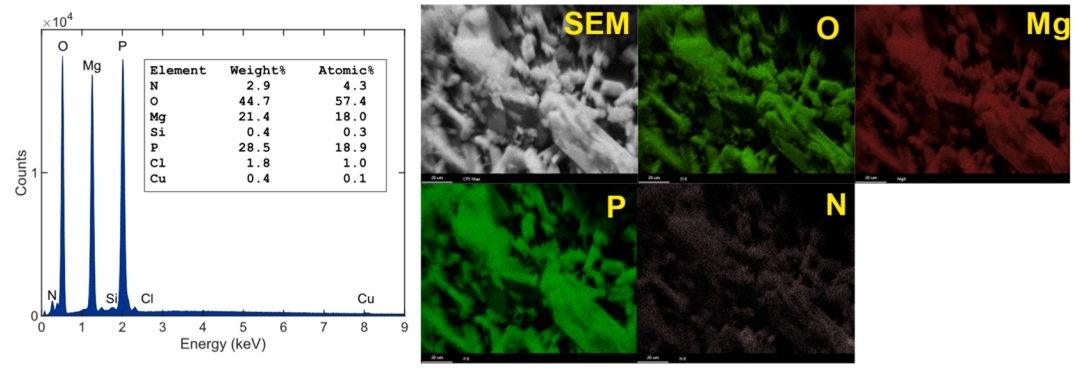

c) Anode

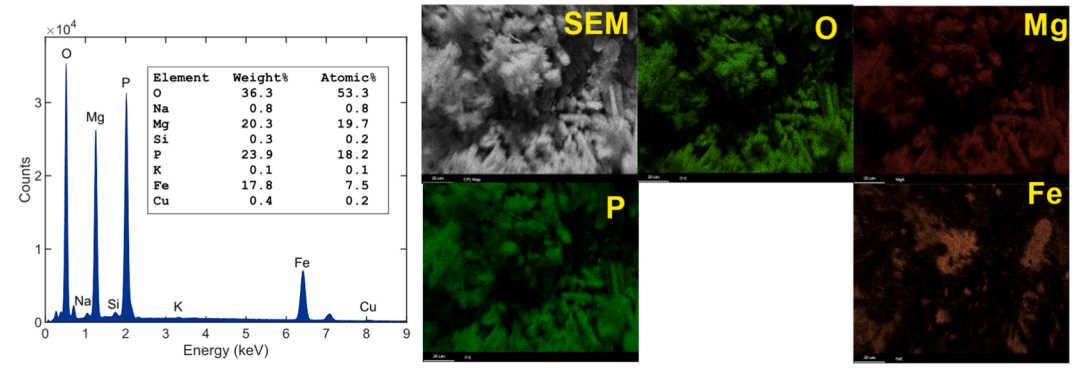

d) Cathode

Fig. 6. EDS spectrum and dot mapping of pure struvite and the obtained precipitates after 3 hr continuous flowcell operation.

3.2. Product characterization

Detailed solid characterization techniques were performed on the precipitates obtained from the continuous flowcell operation to confirm successful struvite formation. Since the characterization results were highly similar across all 3 replicates, only the results of the precipitates obtained from the final replicate are shown.

Comparing XRD patterns (Fig. 4a) of the pure struvite and the recovered precipitates on the anode and in the bulk solution show a strong similarity in both peak positions and relative intensities, indicating the formation of crystals with a structure similar to crystalline struvite. It is worth mentioning that due to a very small amount of solid recovered from the cathode, it was not possible to do XRD even after accumulating solids from all 3 replicates. No additional diffraction peaks were observed relative to the pure struvite standard (COD ID 2106462) for the filtered solids and the anode precipitate, suggesting the absence of detectable secondary crystalline phases and that a high-purity struvite was obtained. However, the XRD pattern of the anode precipitates exhibited one additional low-angle reflection at 2θ approximately 11°, which is not associated with the pure struvite reference. This feature was not observed for the precipitates recovered from the bulk solution.

ATR-FTIR spectra (Fig. 4b) of recovered solids were similar to pure struvite. In particular, the O-H and N-H stretching vibrations are observed as asymmetric broadband peaks in the range 3265–2903 1/cm, corresponding to the presence of structural water molecules and NH_4^+ groups within the struvite lattice [12,45]. Additional bands at approximately 1638 1/cm are attributed to H-O-H bending vibrations, while the sharp peak near 1444 1/cm is associated with N-H bending of the NH_4^+ group [12,45]. The strong absorption band at approximately 983 1/cm corresponds to P–O stretching vibrations of the PO_4^{3-} group, while the band observed near 746 1/cm is associated with lower energy PO_4^{3-} vibrations, including O–P–O bending and P–O stretching modes within the struvite lattice [45]. Other lower wavenumber bands between 893 and 753 1/cm are related to wagging modes of water molecules within the crystal structure [45]. All precipitate samples exhibited the characteristic absorption features shown in Fig. 5, which have previously been reported as diagnostic for pure struvite formation [12,13]. The close agreement of these spectral features with previously reported struvite references indicates that the precipitates recovered from all locations are consistent with high-purity struvite. A clear change in the ATR-FTIR peak pattern is observed when comparing the influent ATR-FTIR spectrum with the struvite samples, demonstrating that the precursor is converted during electrochemical treatment rather than precipitating in its original form after drying.

Preliminary batch/beaker scale experiments at 60 mA using ca. 10 cm^2 pure Mg strips (results not shown here) exhibited pronounced gas evolution at the electrode surfaces, indicating the presence of competing electrochemical reactions and locally elevated pH conditions. Such conditions are known to promote the formation of brucite ($Mg(OH)_2$) due to localized alkalization near electrode surfaces, even when the bulk solution pH remains within the optimal range for struvite formation [7,46]. Under elevated overvoltage or higher current density in preliminary batch/beaker scale experiments, an additional sharp absorption band was observed near 3695 1/cm in the ATR-FTIR spectra (Fig. S4a). This feature was attributed to O–H stretching vibrations of weakly hydrogen-bonded hydroxyl groups characteristic of brucite [47]. In contrast, O–H stretching vibrations in struvite appear as broader bands associated with lattice-bound water molecules [45]. This $Mg(OH)_2$ associated peak at approximately 3695 1/cm was not observed in the ATR-FTIR spectra of the samples obtained from continuous flowcell operation, indicating that the applied process conditions and flow regime limited the formation of localized alkaline environments. The presence of $Mg(OH)_2$ in the precipitates obtained from batch/beaker scale experiments was further supported by XRD analysis (Fig. S4b), as $Mg(OH)_2$ is reported to exhibit an amorphous material characteristic XRD pattern with broad diffraction peaks [47–49]. The low-angle reflection at approximately 11° observed for the anode precipitate from continuous flowcell operation could be related to the formation of mixed-phase struvite containing a small magnesium phosphate impurity, such as cattiite, newberyite, or a small amount of $Mg(OH)_2$. Rietveld refinement and phase fraction assessment relative to other crystalline phases using well-known impurity phases associated with struvite formation [50] revealed struvite as the dominant crystalline phase. The struvite accounted for ca. 85 wt% of the recovered precipitates after 3 hr of continuous flowcell operation from the anode surface (Fig. S5) and the bulk solution (Fig. S6). Minor diffraction features not attributable to struvite indicate the presence of trace phosphate-based impurities. Due to strong structural similarity and peak overlap among hydrated magnesium and ammonium phosphate phases, the individual identity and abundance of these minor phases should be interpreted with caution.

Fig. 5 shows SEM images of the pure struvite and the recovered precipitates. The pure struvite exhibits the expected elongated prismatic morphology with well-defined edges associated with high-purity struvite [7]. The filtered solids, anode, and cathode precipitates predominantly display elongated crystalline features, indicating struvite-type growth rather than amorphous precipitation. This is typically associated with irregular morphology [44]. Inspection of SEM images at different magnifications shows that the pure struvite reference consists of crystals approximately 200 μm in length and around 10 μm in width. Similar inspection of the recovered precipitates indicates crystal lengths in the range of approximately 5–80 μm and widths of about 2–8 μm, with the filtered solids generally consisting of finer crystals compared to the cathode and anode precipitates. The crystal sizes observed in this study fall within the range of previous studies on electrochemical struvite precipitation [7,12–14]. Particle size is important when struvite is intended for use as a fertilizer. Larger crystals are generally preferred because they are easier to handle, transport, and apply to agricultural soil [51]. Previous studies have shown that struvite crystals range between 7 mm and 0.25 μm in length [13]. However, it should be noted that struvite crystals produced electrochemically are usually smaller and typically fall in the range of 50–100 μm in length [7,12,13]. Several conditions influence crystal size, including the degree of supersaturation, reagent concentrations, and other thermodynamic and kinetic factors [13]. Differences in morphology between recovery locations are observed, where the anode precipitate shows more pronounced needle-like crystals, while the cathode precipitate appears more aggregated. These variations are likely related to differences in local supersaturation, hydrodynamic conditions, and electrochemical reactions within the flowcell. This may be explained by the thicker passivation layer observed on the anode surface compared with the cathode after disassembly (Fig. S1). This passivation layer may promote crystal growth by increasing the number of available nucleation sites, as reported in other studies [7,46].

The EDS spectra of pure struvite and recovered precipitates were acquired over an energy range of 0–13 keV (Fig. 6). However, no characteristic peaks were observed above 9 keV. Pure struvite consists of a high fraction of O relative to the other elements and an Mg:P atomic ratio close to unity. Minor impurities are present, with Ca constituting the largest fraction, consistent with the stated 98 % purity of the commercial reference material. Visual inspection of the precipitates showed that the reservoir precipitates were predominantly white, as expected for struvite. In contrast, the precipitates recovered from the cathode and anode exhibited mixed coloration, indicating secondary contributions due to electrode material deposition (Fig. S1). This was most noticeable on the cathode precipitate, which had a reddish coloration originating from oxidized iron. The presence of Fe in the cathode precipitate was confirmed by the EDS analysis, where Fe accounts for an atomic ratio of 7.5 %. This is attributed to the oxidation of the cathode material (untreated steel) after drying. The use of stainless steel would likely reduce this contamination. N was not detected in the cathode sample, which is attributed to instrumental limitations, as N is a light-weight element and

Table 2
Specific electrical energy consumption of the continuous flowcell system.

	kWh	kWh/m^3	kWh/kg$_{\text{struvite produced}}$	kWh/kg$_{PO_4^{3-}\text{ recovered}}$	kWh/kg$_{PO_4^{3-}-P\text{ recovered}}$
Specific electrical energy consumption[1]	7.26×10^{-5}	0.363	0.45	0.55	1.67

Notes: 1- Excluding the energy consumption associated with the 54 W lab scale recirculation pump used in the current lab experiments.

it is difficult to detect by EDS, and its signal can fall below the detection limit when present at low concentrations. In comparison to the pure struvite reference, the N signal in the cathode precipitate was therefore below the detectable range. Overall, the SEM-EDS spectra of the recovered precipitates show a high resemblance to that of the struvite reference, with all expected elements present. The impurity levels, potentially introduced during recovery of precipitates, sample handling, and SEM sample holder/carbon tape in the anode and filtered solids, are comparable to those observed for the commercial reference material, indicating that these samples can be considered chemically pure within the resolution and limitations of SEM-EDS analysis. The most pronounced difference between the reference and the recovered precipitates from the anode and filtered solids is therefore related to crystal size rather than elemental composition. It should be noted that the use of synthetic wastewater in this feasibility study represents a limitation, as under real wastewater conditions, competing ions such as Ca^{2+} and K^{+} may promote the formation of impurities (e.g., hydroxyapatite), potentially leading to the adsorption of organic compounds and requiring careful control of reaction parameters to avoid impurity formation [13,18,50].

3.3. Energy consumption analysis

The specific energy consumption of the continuous electrochemical flowcell system is summarized in Table 2. To enable comparison with studies employing beaker-type batch reactors, the results are reported excluding energy for pumping. When excluding the pump and considering only the DC power supply consumption (1.2 V, 20 mA), the specific energy demand of the system (0.45 kWh/kg$_{\text{struvite produced}}$) falls within the same order of magnitude as values reported for beaker-type batch electrochemical reactors in the literature [14,52]. To this must be added the specific energy consumption for the recirculation pump. This increase in energy consumption depends on the full scale optimized hydraulic design of the continuous electrochemical flowcell system, appropriate pipeline sizing, proper pump selection, and sizing based on influent pressure, overall stack pressure drop, and net positive suction head (NPSH). It can thus only be stated with any reliable accuracy when a full-scale flowcell and overall process design have been made.

4. Conclusion

This research highlights the successful continuous production of value-added struvite ($MgNH_4PO_4$) from synthetic wastewater at pre-pilot scale using a filter-press electrochemical flowcell. The process was conducted in full-recirculation mode for 3 hr at a flowrate of 0.62 L/min to promote turbulence within the reactor and over the electrode surfaces. The reaction conditions were pH 8.5 with a current density of 1.7 mA/cm^2 based on previous literature. A PO_4^{3-} recovery of 84.4 $\pm$ 0.2 % was achieved, and the struvite yield was 40 $\pm$ 3 %. Struvite precipitates were observed on the anode (24 $\pm$ 2 %), in the bulk solution (14 $\pm$ 2 %), and on the cathode (2.1 $\pm$ 0.7 %), indicating that the turbulent flow regime effectively swept some of the precipitates from the anode surface. The successful struvite formation was confirmed using ATR-FTIR, SEM-EDS, and XRD, and the results were compared with those of pure struvite. The analyses confirmed that the obtained struvite product matched the characteristics of pure struvite. Future research should investigate additional optimization strategies, such as pulsating current, continuous pH adjustment, the influence of higher flowrate/turbulency, intermittent or reverse flow, and intermittent air burst sparging within the flowcell channel, to enhance the removal of struvite precipitates from the anode surface, thus eliminating the struvite passivating layer formed on the anode surface. Moreover, sensitivity analyses of key operational parameters such as flow rate, pH, current density, long-term stability assessments involving extended operation times and consecutive cycles, optimizing ion-selective transport using membranes, and scale-up studies using multicell stack configurations, should be considered for future scale-up evaluation. The study underscores the adaptability of electrochemical filter-press flowcells, which can be expanded to multiple stacks and reactors in series/parallel to meet the required feed flowrate and residence time. Future work may also explore integrating the proposed scalable flowcell concept into a Mg–air cell system. This research establishes a foundation for advancing the simultaneous valorization and treatment of real process and urban wastewater through a green and continuous pilot-scale process, which can be integrated into multi-step wastewater treatment plants.

CRediT authorship contribution statement

Per Morgen: Writing – review & editing, Software, Resources, Investigation, Formal analysis, Data curation. **Massimiliano Errico:** Writing – review & editing, Validation, Supervision, Resources, Project administration, Methodology, Funding acquisition, Conceptualization. **Knud Villy Christensen:** Writing – review & editing, Supervision, Resources, Project administration, Funding acquisition. **Benjamin Rommelhoff Høy:** Writing – review & editing, Writing – original draft, Visualization, Methodology, Investigation, Formal analysis, Data curation. **Soorena Gharibian:** Writing – review & editing, Writing – original draft, Visualization, Validation, Supervision, Project administration, Methodology, Investigation, Formal analysis, Data curation, Conceptualization.

Declaration of Competing Interest

The authors declare the following financial interests/personal relationships which may be considered as potential competing interests: Massimiliano Errico reports financial support was provided by European Commission. If there are other authors, they declare that they have no known competing financial interests or personal relationships that could have appeared to influence the work reported in this paper.

Acknowledgements

The authors would like to extend their gratitude to SDU Research & Innovation Organisation (SDU RIO) and the MakerSpace team for providing training and access to the 3D printing setup. This project has received funding from Horizon Europe, the European Union's Framework 627 Programme for Research and Innovation, under Grant Agreement No. 101122363 (SUSTEPS). Views and opinions expressed are, however, those of the authors only and do not necessarily reflect those of the European Union or the granting authority, CINEA. Neither the European Union nor CINEA can be held responsible for them

Appendix A. Supporting information

Supplementary data associated with this article can be found in the online version at doi:10.1016/j.jece.2026.121922.

Data availability

Data will be made available on request.

References

[1] D. Cordell, S. White, Peak phosphorus: clarifying the key issues of a vigorous debate about long-term phosphorus security, Sustainability 3 (10) (2011) 2027–2049.
[2] M. Grohol, C. Veeh. Study on the Critical Raw Materials for the EU, Publications Office of the European Union, 2023.
[3] A. Reichelt-Brushett, Marine Pollution–monitoring, Management and Mitigation, Springer Nature, 2023.
[4] J. Watson, et al., Valorization of hydrothermal liquefaction aqueous phase: pathways towards commercial viability, Prog. Energy Combust. Sci. 77 (2020) 100819.
[5] L. Leng, et al., Use of microalgae to recycle nutrients in aqueous phase derived from hydrothermal liquefaction process, Bioresour. Technol. 256 (2018) 529–542.
[6] T.M. Edwards, et al., Ammonia and aquatic ecosystems–a review of global sources, biogeochemical cycling, and effects on fish, Sci. Total Environ. 907 (2024) 167911.
[7] L. Kékedy-Nagy, et al., Electrochemical removal and recovery of phosphorus as struvite in an acidic environment using pure magnesium vs. the AZ31 magnesium alloy as the anode, Chem. Eng. J. 380 (2020).
[8] C.A. Cid, J.T. Jasper, M.R. Hoffmann, Phosphate recovery from human waste via the formation of hydroxyapatite during electrochemical wastewater treatment, ACS Sustain. Chem. Eng. 6 (3) (2018) 3135–3142.
[9] B. Sniatala, et al., Macro-nutrients recovery from liquid waste as a sustainable resource for production of recovered mineral fertilizer: uncovering alternative options to sustain global food security cost-effectively, Sci. Total Environ. 856 (2023) 159283.
[10] Y. Zheng, et al., Recovery of phosphorus from wastewater: a review based on current phosphorous removal technologies, Crit. Rev. Environ. Sci. Technol. 53 (11) (2023) 1148–1172.
[11] C.Y. Sousa, et al., Phosphorus recovery from industrial effluents through chemical and electrochemical precipitation: a critical review, Rev. Environ. Sci. Bio/Technol. (2025) 1–22.
[12] L. Kékedy-Nagy, et al., The effect of anode degradation on energy demand and production efficiency of electrochemically precipitated struvite, J. Appl. Electrochem. 52 (2) (2021) 205–215.
[13] L. Kékedy-Nagy, et al., Sustainable electroless nutrient recovery from natural agro-industrial and livestock farm wastewater effluents with a flow cell reactor, Resour. Conserv. Recycl. 212 (2025).
[14] R. Sultana, et al., Electrochemical recovery of phosphate from synthetic wastewater with enhanced salinity, Electrochim. Acta 426 (2022).
[15] S. Esteki, et al., Application of an electrochemical filter-press flowcell in an electrocoagulation-MBR system: efficient membrane fouling mitigation, J. Environ. Chem. Eng. 12 (1) (2024).
[16] X. Zhou, Y. Chen, An integrated process for struvite electrochemical precipitation and ammonia oxidation of sludge alkaline hydrolysis supernatant, Environ. Sci. Pollut. Res. 26 (3) (2019) 2435–2444.
[17] G.P. Bhoi, K.S. Singh, D.A. Connor, Optimization of phosphorus recovery using electrochemical struvite precipitation and comparison with iron electrocoagulation system, Water Environ. Res. 95 (4) (2023) e10847.
[18] H. Sudibyo, et al., Thermodynamics and kinetics of struvite crystallization from hydrothermal liquefaction aqueous-phase considering hydroxyapatite and organics coprecipitation, Ind. Eng. Chem. Res. 61 (20) (2022) 6894–6908.
[19] M. Muys, et al., A systematic comparison of commercially produced struvite: quantities, qualities and soil-maize phosphorus availability, Sci. Total Environ. 756 (2021) 143726.
[20] A. Gysin, D. Lycke, S. Wirtel, The Pearl® and WASSTRIP® processes (Canada), in: C. Schaum (Ed.), Phosphorus: Polluter and Resource of the Future, IWA Publishing, London, 2018, pp. 359–366.
[21] S. Agrawal, J.S. Guest, R.D. Cusick, Elucidating the impacts of initial supersaturation and seed crystal loading on struvite precipitation kinetics, fines production, and crystal growth, Water Res. 132 (2018) 252–259.
[22] J.A. Wilsenach, C.A. Schuurbiers, M.C. van Loosdrecht, Phosphate and potassium recovery from source separated urine through struvite precipitation, Water Res. 41 (2) (2007) 458–466.
[23] K.R. Brye, et al., Assessment of struvite as an alternative sources of fertilizer-phosphorus for flood-irrigated rice, Sustainability 14 (15) (2022) 9621.
[24] K.G. Morrissey, et al., Prospective life cycle assessment and cost analysis of novel electrochemical struvite recovery in a US wastewater treatment plant, Sustainability 14 (20) (2022) 13657.
[25] X. Wu, et al., Recovery of phosphate and ammonium nitrogen as struvite from aqueous solutions using a magnesium–air cell system, Sci. Total Environ. 819 (2022) 152006.
[26] L. Kékedy-Nagy, et al., The effect of anode degradation on energy demand and production efficiency of electrochemically precipitated struvite, J. Appl. Electrochem. 52 (2) (2022) 205–215.
[27] F. Wang, et al., Phosphate recovery from swine wastewater by a struvite precipitation electrolyzer, Sci. Rep. 9 (1) (2019) 8893.
[28] S. Gharibian, H. Hazrati, Towards practical integration of MBR with electrochemical AOP: Improved biodegradability of real pharmaceutical wastewater and fouling mitigation, Water Res. 218 (2022) 118478.
[29] S. Gharibian, H. Hazrati, M. Rostamizadeh, Continuous electrooxidation of Methylene Blue in filter press electrochemical flowcell: CFD simulation and RTD validation, Chem. Eng. Process. Process. Intensif. 150 (2020).
[30] S. Gharibian, et al., Homogenous Electro-Fenton degradation of phenazopyridine in wastewater using a 3D Printed filter-press flowcell: optimization via response surface methodology, J. Taiwan Inst. Chem. Eng. 170 (2025).
[31] R. Granados-Fernández, A. Cárdenas-Arenas, M.A. Montiel, Revolutionizing lab-scale electrochemical reactors: innovative breakthroughs with 3D printing fabrication, ChemElectroChem 11 (15) (2024) e202400205.
[32] O.M. Cornejo, et al., Recent advances in electrochemical flow reactors used in advanced oxidation processes: a critical review, Chem. Eng. J. 496 (2024) 153935.
[33] F. Franco, et al., A systematic performance history analysis of a chlor-alkali membrane electrolyser under industrial operating conditions, Appl. Sci. 9 (2) (2019) 284.
[34] H. Zhang, Y. Zuo, J. Huang, Green hydrogen from alkaline water electrolysis: bridging the gaps between laboratory research and industrial applications, Chem. Synth. 5 (3) (2025) (p. N/A-N/A).
[35] F.F. Rivera, et al., The filter-press FM01-LC laboratory flow reactor and its applications, Electrochim. Acta 163 (2015) 338–354.
[36] T. Pérez, et al., Simulation of current distribution along a planar electrode under turbulent flow conditions in a laboratory filter-press flow cell, Electrochim. Acta 154 (2015) 352–360.
[37] S. Shahgodari, J. Llorens, J. Labanda, Study of total ammoniacal nitrogen recovery using polymeric thin-film composite membranes for continuous operation of a hybrid membrane system, Polymers 17 (12) (2025) 1696.
[38] K. Emerson, et al., Aqueous ammonia equilibrium calculations: effect of pH and temperature, J. Fish. Board Can. 32 (12) (1975) 2379–2383.
[39] K. Momma, F. Izumi, VESTA 3 for three-dimensional visualization of crystal, volumetric and morphology data, Appl. Crystallogr. 44 (6) (2011) 1272–1276.
[40] S. Gražulis, et al., Crystallography Open Database–an open-access collection of crystal structures, Appl. Crystallogr. 42 (4) (2009) 726–729.
[41] N. Doebelin, R. Kleeberg, Profex: a graphical user interface for the Rietveld refinement program BGMN, Appl. Crystallogr. 48 (5) (2015) 1573–1580.
[42] R.C. de Souza Meira, S.P.A. da Paz, J.A.M. Corrêa, XRD-Rietveld analysis as a tool for monitoring struvite analog precipitation from wastewater: P, Mg, N and K recovery for fertilizer production, J. Mater. Res. Technol. 9 (6) (2020) 15202–15213.
[43] A. Rabinovich, A.A. Rouff, Effect of phenolic organics on the precipitation of struvite from simulated dairy wastewater, ACS EST Water 1 (4) (2021) 910–918.
[44] Y. Song, et al., Nutrients removal and recovery by crystallization of magnesium ammonium phosphate from synthetic swine wastewater, Chemosphere 69 (2) (2007) 319–324.
[45] V. Stefov, et al., Infrared and Raman spectra of magnesium ammonium phosphate hexahydrate (struvite) and its isomorphous analogues. I. Spectra of protiated and partially deuterated magnesium potassium phosphate hexahydrate, J. Mol. Struct. 689 (1) (2004) 1–10.
[46] C.M. Mehta, D.J. Batstone, Nucleation and growth kinetics of struvite crystallization, Water Res. 47 (8) (2013) 2890–2900.
[47] S. Yousefi, B. Ghasemi, M.P. Nikolova, Opto-structural characterization of Mg(OH) 2 and MgO nanostructures synthesized through a template-free sonochemical method, Appl. Phys. A 127 (7) (2021).
[48] G. Chen, et al., Crosslinking ionic oligomers sol-gel synthesis of porous amorphous magnesium hydroxide and its application in Pb2+ adsorption, J. Solid State Chem. 345 (2025) 125214.
[49] C. Shaw, et al., Using magnesium hydroxide for ocean alkalinity enhancement: elucidating the role of formation conditions on material properties and dissolution kinetics, Author Prepr. (2025).
[50] B. Tansel, G. Lunn, O. Monje, Struvite formation and decomposition characteristics for ammonia and phosphorus recovery: a review of magnesium-ammonia-phosphate interactions, Chemosphere 194 (2018) 504–514.
[51] B. Li, et al., Phosphorous recovery through struvite crystallization: challenges for future design, Sci. Total Environ. 648 (2019) 1244–1256.
[52] A. Hug, K.M. Udert, Struvite precipitation from urine with electrochemical magnesium dosage, Water Res. 47 (1) (2013) 289–299.